Biogeosciences Discuss., 11, 1443–1478, 2014
www.biogeosciences-discuss.net/11/1443/2014/
doi:10.5194/bgd-11-1443-2014

Biogeosciences Discussions
Open Access

An ensemble approach to simulate CO_2 emissions from natural fires

A. V. Eliseev, I. I. Mokhov, and A. V. Chernokulsky

A. M. Obukhov Institute of Atmospheric Physics RAS, Moscow, Russia

Received: 8 November 2013 – Accepted: 6 January 2014 – Published: 22 January 2014

Correspondence to: A. V. Eliseev (eliseev@ifaran.ru)

Published by Copernicus Publications on behalf of the European Geosciences Union.

Abstract

This paper presents ensemble simulations with the global climate model developed at the A. M. Obukhov Institute of Atmospheric Physics, Russian Academy of Sciences (IAP RAS CM). These simulations were forced by historical reconstruction of external forcings for 850–2005 AD and by the Representative Concentration Pathways (RCP) scenarios till year 2300. Different ensemble members were constructed by varying the governing parameters of the IAP RAS CM module to simulate natural fires. These members are constrained by the GFED–3.1 observational data set and further subjected to Bayesian averaging. This approach allows to select only changes in fire characteristics which are robust within the constrained ensemble. In our simulations, the present-day (1998–2011 AD) global area burnt due to natural fires is $(2.1 \pm 0.4) \times 10^6$ km^2 yr^{-1} (ensemble means and intra-ensemble standard deviations are presented), and the respective CO_2 emissions in the atmosphere are (1.4 ± 0.2) PgC yr^{-1}. The latter value is in agreement with the corresponding observational estimates. Regionally, the model underestimates CO_2 emissions in the tropics; in the extra-tropics, it underestimates these emissions in north-east Eurasia and overestimates them in Europe. In the 21st century, the ensemble mean global burnt area is increased by 13 % (28 %, 36 %, 51 %) under scenario RCP 2.6 (RCP 4.5, RCP 6.0, RCP 8.5). The corresponding global emissions increase is 14 % (29 %, 37 %, 42 %). In the 22nd–23rd centuries, under the mitigation scenario RCP 2.6 the ensemble mean global burnt area and respective CO_2 emissions slightly decrease, both by 5 % relative to their values in year 2100. Under other RCP scenarios, these variables continue to increase. Under scenario RCP 8.5 (RCP 6.0, RCP 4.5) the ensemble mean burnt area in year 2300 is higher by 83 % (44 %, 15 %) than its value in year 2100, and the ensemble mean CO_2 emissions are correspondingly higher by 31 % (19 %, 9 %). All changes of natural fire characteristics in the 21st–23rd centuries are associated mostly with the corresponding changes in boreal regions of Eurasia and North America. However, under the RCP 8.5 scenario, increase of the burnt area and CO_2 emissions in boreal

BGD
11, 1443–1478, 2014

regions during the 22nd–23rd centuries are accompanied by the respective decreases in the tropics and subtropics.

1 Introduction

One of the most important recent achievements in global environmental modelling is an implementation of biogeochemistry modules in global climate models which converted the latters to Earth system models. A substantial part of the terrestrial biogeochemistry modules is a scheme simulating natural fires. The first such scheme was the Glob–FIRM (Global FIRe Model) (Thonicke et al., 2001). This scheme is based on statistical description of natural fires relating their bulk characteristics (length of fire season, burnt area, and carbon emissions) to environmental variables (soil moisture content and carbon stocks) via specified functional relationships. Currently, this model is a part of the LPJ (Lund–Potsdam–Jena) terrestrial vegetation model (Sitch et al., 2003). It was followed by the schemes developed at the Canadian Centre for Climate Modelling and Analysis (CCCMA) (Arora and Boer, 2005) and at the National Center for Atmospheric Research (NCAR) (Pechony and Shindell, 2009). Comparing to the Glob–FIRM model, the latter two schemes account for (i) an impact of both natural and anthropogenic ignition sources on fire occurrence, (ii) an influence of wind direction and speed on fire propagation. These two schemes were implemented in the respective global climate models and, in a slightly changed version, in the CLM–3.1 land-surface model (Common Land Model, version 3.5) (Kloster et al., 2010, 2012). Li et al. (2012) developed an intermediate complexity scheme to calculate characteristics of natural fires, which is based on both the CCCMA and NCAR schemes. Up to the date, the most advanced scheme for simulation of natural fires in global climate models is the SPITFIRE model (Thonicke et al., 2010) which is able to calculate even the detailed characteristics of natural fires.

We note also that there is an alternative impact-oriented approach to study natural fires based on climatic indices (e.g., de Groot et al., 2007; Dowdy et al., 2010; Mokhov

BGD
11, 1443–1478, 2014

et al., 2006; Mokhov and Chernokulsky, 2010). The latter is based on climate-based indices of fire danger, which differs somewhat in different countries (e.g., Nesterov, 1949; Noble et al., 1980; Van Wagner, 1987). This approach is well-tested empirically, but lacks information on burnt area and associated emissions of atmospheric constituents.

At the day, the global-scale natural fire modelling is far from its maturity stage. As a result, the values of some important parameters are known with insufficient precision, and frequently they just tuned to achieve a reasonable performance of a particular model. In the present paper, we suggest an approach to partially overcome this shortcoming: to sample relevant governing parameters, constrain these simulations by available observations, calculate ensemble statistics, and consider ensemble means and standard deviations as proxies for true values of characteristics of natural fires and their uncertainties, respectively (Fig. 1). To put these simulations in the context of the contemporary climate change and climate change expected in the next few centuries, we force our model by anthropogenic scenarios prepared for the CMIP5 (Coupled Models Intercomparison Project, phase 5) till the end of the 23rd century. We note that, while the "core" CMIP5 simulations end in 2100 AD, the "tier 1" and "tier 2" ones are extended till year 2300 (Taylor et al., 2012). In all these simulations, the anthropogenic forcing is stabilised not later than in the mid-22nd century, but climate inertia may lead to pronounced changes in climate state for decades and even centuries after such a stabilisation, and, consequently, to changes in characteristics of natural fires. So, it is profitable to extend our simulations for the whole period covered by the CMIP5 scenarios to study possible impact of delayed climate changes on simulation of natural fires. Large computation burden, involved in our exercise, precludes to use the detailed state-of-the-art climate model, and we use the global climate model of intermediate complexity. In turn, because the latter model is unable to provide a necessary information for the detailed scheme for simulating natural fires, we use a simplified (albeit realistic at global and continental scales) natural fire module, which is a descendant of the Glob–FIRM model.

BGD
11, 1443–1478, 2014

2 Methods

2.1 IAP RAS global climate model

In this paper, the global climate model developed at the A.M. Obukhov Institute of Atmospheric Physics, Russian Academy of Sciences (Petoukhov et al., 1998; Mokhov et al., 2002, 2005; Mokhov and Eliseev, 2012) was used. It belongs to the class of Earth system models of intermediate complexity (Claussen et al., 2002; Petoukhov et al., 2005; Eby et al., 2013; Zickfeld et al., 2013). Initial implementation of the natural fire module as a part of the IAP RAS CM's terrestrial carbon cycle module is described by Eliseev and Mokhov (2011). In the present paper, the IAP RAS CM fire module was extended and retuned. This was motivated by modifications included in the IAP RAS terrestrial carbon cycle model relative to (Eliseev and Mokhov, 2011). The first modification concerns an accounting of diffuse radiation on intensity of terrestrial photosynthesis (Eliseev, 2012). The second improvement is due to implementation of co-existing multiple plant functional types (PFTs) in the same grid cell (Eliseev and Sergeev, 2014).

The model's terrestrial vegetation module distinguishes seven plant functional types (PFTs): tropical trees, temperate broadleaf trees, cool needleleaf trees, grasses, shrubs, wetlands, and crops. To allow two or more PFTs co-exist in a model grid cell, a mosaic approach is used. Fractional areas occupied by PFTs are prescribed and do not respond to natural fire activity in the model. However, they are allowed to evolve in time according to the external deforestation/afforestation scenario. Terrestrial gross primary production depends on climate conditions (represented by the downwelling photosynthetically-active radiation, fraction of diffuse radiation in the latter flux, surface air temperature, temperature and moisture content of the upper 50 cm soil layer) and on the CO_2 atmospheric content. Seasonal changes of all input variables are considered explicitly, but all output variables are annual means in order to preserve the well-mixed-gas approximation for the atmospheric CO_2. Vegetation carbon is divided in two pools: the "leave" pool representing leaves, thin branches and thin roots, and

BGD
11, 1443–1478, 2014

the "wood" pool representing thick branches, thick roots, and hardwood. The litter fall from the "leave" pool is assumed to enter the fast soil carbon pool, where organics is decomposed with a typical time scale of several years. The litter from the "wood" pool is assumed to enter the slow carbon soil pool, which time of decomposition is of the order several tens of years. Both these decomposition rates depend on soil temperature and soil moisture content. Two types of vegetation disturbance are considered: natural fires and land use clearing. The latter results in direct land use CO_2 emissions which are calculated interactively by the model. Riverine carbon fluxes are currently neglected. An explicit interaction of carbon cycle with other biogeochemical cycles (e.g., nitrogen or phosphorous cycles) is currently neglected as well.

The model implements a statistical module to simulate characteristics of natural fires, which is a descendant of the GlobFIRM model (Thonicke et al., 2001). In this model, the fractional (relative to the area occupied by a given PFT in a given grid cell) burnt area is calculated as a function of soil moisture and available fuel stock. The whole "leave" carbon pool in this burnt part of the cell is consumed completely during fires. The respective amount of the consumed "wood" pool depends on PFT in a way similar to that used by Thonicke et al. (2001) (see Eliseev and Sergeev, 2014, for more details).

For the present paper, the model's natural fires module is extended by a simple parametrisation of peat fires. If, during time step and in a given grid cell, natural fires consume vegetation carbon mass per unit area δc_v, they also consume carbon in soil. The latter consumption per unit area in our model is applied only if the total soil carbon stock is larger than $10\,\mathrm{kgC\,m^{-2}}$ and reads

$$\delta c_s = \alpha_{f,s}\delta c_v(1 - W), \quad (1)$$

where $\alpha_{f,s}$ is PFT-dependent coefficient, and W is moisture fractional saturation of the upper soil level. The threshold value to apply this consumption ($10\,\mathrm{kgC\,m^{-2}}$) was chosen as a typical value distinguishing the peat and non-peat soils. When burnt, both δc_s and δc_v are assumed to be emitted in the atmosphere in the form of carbon dioxide. As a result, total CO_2 emissions per unit area in the atmosphere due to natural fires

BGD
11, 1443–1478, 2014

read

$$e = e_v + e_s, \quad (2)$$

and

$$e_v = \delta c_v \quad (3)$$
$$e_s = \delta c_s.$$

2.2 Simulations

Our simulations follow the CMIP5 (Coupled Model Intercomparison Project, phase 5) protocol (Taylor et al., 2012). In particular, we have performed "historic" simulations forced by the forcing reconstructions for 850–2005 AD. This simulation was initialised from the model state occurring after 200 yr spin-up with the forcing values corresponding to year 850 AD. This simulation was continued till year 2300 forced by the Representative Concentration Pathways (RCPs) scenarios. All scenarios RCP 2.6, RCP 4.5, RCP 6.0, and RCP 8.5 (see Moss et al., 2010) were used in our paper. We emploied forcings due to three well-mixed atmospheric greenhouse gases (GHGs; namely, CO_2, N_2O, and CH_4), tropospheric and stratospheric sulphate aerosols (only direct forcing), change in surface albedo due to land use, and total solar irradiance. For carbon dioxide, we prescribed fossil fuel + industrial CO_2 emissions and computed the respective land use emissions by the model's terrestrial carbon cycle scheme based on change of extent of crops and pastures. Carbon dioxide content in the atmosphere was calculated interactively by the IAP RAS CM as well. For other well-mixed GHGs (N_2O and CH_4) atmospheric concentrations were used to force the model. Orbital forcing, possible change in vegetation types under climate changes, and changes in ozone burdens in the stratosphere and troposphere were neglected. Ice sheets distribution and heights were prescribed in the model.

All simulations were performed in an ensemble manner by varying governing parameters of the natural fires module implemented in the IAP RAS CM:

BGD
11, 1443–1478, 2014

– Fraction $m_{\text{f, wood}}$ of carbon stock in hardwood and thick branches and thick woods consumed during fires. This parameter controls vegetation fuel stock available for fires:

$$c_{\text{fuel}} = c_{\text{leaf}} + m_{\text{f, wood}} c_{\text{wood}}, \quad (4)$$

where c_{leaf} is carbon stock in leaves and thin branches and roots, and c_{wood} is its counterpart in hardwood and thick branches and roots.

– Parameter $c_{\text{fuel},0}$, which is a threshold of fuel availability for natural fires, below which these fires do not develop. In turn, the fuel stock is calculated as a linear function of carbon stock in leaves, fine branches and fine roots.

– Moisture of extinction W_{e} which controls the probability of fires to occur.

– Plant resistance to fire k_{res} relating CO_2 emissions from living vegetation due to natural fires, e_{v}, and burnt vegetation fuel stock:

$$e_{\text{v}} = \delta c_{\text{v}} = k_{\text{res}} c_{\text{fuel}}. \quad (5)$$

– coefficient $\alpha_{\text{f, s}}$ in Eq. (1).

All listed parameters were sampled by the Latin Hypercube sampling (McKay et al., 1979; Stein, 1987). Their ranges and standard values were adopted in the IAP RAS CM are listed in Table (1). The total sample size was $K = 30$.

Thereafter, performed simulations are labelled according to anthropogenic scenarios for the 21st–23rd centuries.

2.3 Post–processing

A Bayesian averaging of individual ensemble members (Kass and Raftery, 1995; Leroy, 1998; Hoeting et al., 1999) is employed in the present work. In particular, for each

BGD
11, 1443–1478, 2014

model variable or parameter Y, ensemble mean $\mathcal{E}(Y|D)$ and ensemble standard deviation $\sigma(Y|D)$, both conditioned by data set D, are computed, respectively, as follows:

$$\mathcal{E}(Y|D) = \sum_{k=1}^{K} Y_k w_k \tag{6}$$

and

$$\sigma(Y|D) = \left\{ \sum_{k=1}^{K} \left[\sigma_k^2 + Y_k^2 \right] w_k - \mathcal{E}(Y|D)^2 \right\}. \tag{7}$$

Here Y_k is output for the ensemble member M_k ($k = 1, \ldots, K$), σ_k is standard deviation of natural variability generated by the model, w_k is the weight attached to this ensemble member. Because our model, similar to other Earth system models of intermediate complexity, underestimates natural variability, we set $\sigma_k = 0$ in Eq. (7).

Bayesian weights w_k's are calculated by comparing the modelled emissions due to natural fires e with their observational counterparts. These weights are constructed based on two figures depicting global total emissions, $w_{g,k}$, and spatial structure of fire emissions, $w_{s,k}$:

$$w_k \propto w_{g,k} w_{s,k}. \tag{8}$$

The first is calculated assuming normal distribution of modelling bias in E_g (here and below E depicts the value of e_f summed over a given region and the subscript indicates this region, "global" in the present example):

$$w_{g,k} = \left(2\pi\sigma_{g,o}^2 \right)^{-1/2} \exp\left(-\frac{\left(E_g - E_{g,o} \right)^2}{2\sigma_{g,o}^2} \right). \tag{9}$$

BGD
11, 1443–1478, 2014

Here the subscript "o" stands for the observed values, $\sigma_{g,o}$ is sampled standard deviation of global CO_2 emissions due to natural fires. In turn, $w_{k,s}$ is computed as in (Taylor, 2001):

$$w_{s,k} = \frac{(1+r)^4}{\left(a_{rel}^2 + a_{rel}^{-2}\right)}. \quad (10)$$

In Eq. (10), r is the coefficient of spatial correlation between area weighted modelled and observed fields of CO_2 emissions due to fires, and a_{rel} is the so called relative spatial variation which reads

$$a_{rel} = a/a_o \quad (11)$$

where a^2 is the spatially (area weighted) average of $\left(e - E_g/A_g\right)^2$, and A_g is the area of the Earth surface. In turn, a_o is defined similar to a but for the observed field. To apply Eqs. (6) and (7), weights are standardised assuring that $\sum_{k=1}^{K} w_k = 1$.

The GFED–3.1 (Global Fire Emission Database, version 3.1, see van der Werf et al., 2010) for years 1997–2010 data set is used to compute the Bayesian weights. Only natural fires (classified either "grassland and open savanna fires" or "woodland fires" or "forest fires" or "peat fires" in this database) are used to calculate the Bayesian weights. In addition, because CO_2 emissions due to peat fires were extremely large in year 1997 (0.7 $PgC\,yr^{-1}$ while in other years they never exceeded 0.2 $PgC\,yr^{-1}$), we redid all our calculations excluding year 1997 from the computation of Bayesian weights. No marked differences between these two approaches were found, and further all results are presented for Bayesian weights calculated for 1998–2010 AD. According to GFED–3.1 data, $E_{g,o} = 1.4\,PgC\,yr^{-1}$, and $\sigma_{g,o} = 0.2\,PgC\,yr^{-1}$. These numbers were used in Eq. (9) to obtain $w_{g,k}$.

Once calculated based on the data for 1997–2011 AD, the Bayesian weights are used to weight the members of the constructed ensemble for the whole simulation

BGD
11, 1443–1478, 2014

length. This is based on the assumption which is common for many ensemble–based projections: the members, which are sufficiently successful in reproducing available observations, are considered to be the most realistic for future changes as well (Kass and Raftery, 1995; Leroy, 1998; Hoeting et al., 1999; Greene et al., 2006; Kattsov et al., 2007; Khon et al., 2010; Arzhanov et al., 2012). For our model, as well as for other process–based models, this assumption might be heuristically justified by indicating that the processes, which are believed to be most important for the problem at hand, are implemented in the model, and the Bayesian approach is used only to calibrate the governing parameters of the model. In addition, we note that there is always a lot of subjectivity in the choice of the cost function which is used to calculate weights of individual ensemble members. Nevertheless, thus constructed Bayesian projections are meaningful for future projections of the environmental system (Kass and Raftery, 1995; Leroy, 1998; Hoeting et al., 1999; Greene et al., 2006; Eliseev, 2008, 2011; Arzhanov et al., 2012). To reduce an uncertainty related to the specific details of Bayesian weighting, we also made a projection, in which all the members with weights $w_k \le 1/K$ are dropped and only the sufficiently successful members are retained. Both qualitative and quantitative results are very similar between these two projections (compare Figs. 2–6 and S2–S6). Hence, we may conclude that the basic results of our paper are not sensitive to the Bayesian weighting specifics. However, intra-ensemble standard deviation becomes smaller if ensemble members with small weights are excluded from averaging. Further, only the original Bayesian averaging is discussed.

Thereafter, change of variable Y between different time periods, ΔY, is considered to be robust within the ensemble under study if magnitude of ensemble mean for this change is at least twice as large as the respective intra-ensemble standard deviation (Eliseev, 2011; Arzhanov et al., 2012):

$$|\mathcal{E}(\Delta Y|D)| \ge 2 \times \sigma(\Delta Y|D). \quad (12)$$

Below, we report only ensemble mean changes which are robust within the constructed ensemble.

BGD
11, 1443–1478, 2014

Thereafter, we test our simulations against the GFED–3.1 data. We note, however, that these data, strictly speaking, contain information on all fires (both natural and anthropogenic), while we simulate only natural fires. Nevertheless, CO_2 emissions may be compared directly, because the GFED data contain fractions of emissions attributed to different sources. Unfortunately, no such information is available for the burnt area. In principle, we could get relevant estimates taking into account the change of crop and pastures extent in time. However, this approach would overlook fires due to the agricultural waste burn (which is, probably, of minor importance) and tacitly assume that (i) all change of extent of crops and pastures is due to deforestation, and (ii) all cut wood is burnt. Both assumptions (i) and (ii) are incorrect (e.g., Houghton et al., 2012, and references therein). This is the reason why we have mostly limited our comparison to the carbon dioxide emissions in the atmosphere, and report only the model numbers on the burnt area. However, the simulated burnt area in the boreal zone are compared with the estimates by Conard et al. (2002).

3 Results

3.1 Calibrated values of governing parameters

The Bayesian weights for individual ensemble members are shown in Fig. S1. It is evident from this Figure that our ensemble is dominated by a few members. In particular, only four Bayesian weights are larger than $1/K = 1/30$, which is the value for the equally–weighted averaging. Only ten ensemble members have weights larger than 0.01. Total weights w_k are closely related to $w_{g,k}$. In particular, the pairwise intra-ensemble Pearson correlation coefficients between w_k and $w_{g,k}$ equals to 0.99. In turn, the corresponding correlation coefficient between w_k and $w_{s,k}$ is only 0.15, which is statistically insignificant assuming that our ensemble weights are mutually independent (this assumption is well–provided because of the Latin Hypercube sampling) and sampled from the normal probability distribution (this assumption can not be tested

BGD
11, 1443–1478, 2014

here because of insufficient sample size). Even smaller (equal to 0.12) correlation coefficient is found between $w_{g,k}$ and $w_{s,k}$. The latter allows to consider $w_{g,k}$ and $w_{s,k}$ as variables which mutually statistically independent, and, therefore, to use Eq. (8) to calculate the Bayesian weights.

We have "calibrated" governing parameter based on our ensemble simulations. This is done by the method suggested by Eliseev et al. (2013) where such a calibration was done by employing the Bayesian averaging (Eqs. 6 and 7) but using parameter values in place of Y. In so doing, the Bayesian ensemble mean is considered as a central value, and the Bayesian intra-ensemble standard deviation is used as a substitute of width of a range in which the simulation results are close to those obtained with a central parameter set.

The obtained values are shown in Table 1. All simulations with sufficiently large weights are characterised by moisture of extinction, W_e, which is close to 0.56. For instance, the ensemble members with $w_k \geq 0.01$ (which is approximately one third of $1/K$) have $0.53 \geq W_e \geq 0.68$. However, the left tail of the posterior distribution for W_e is substantially shorter than the right one. The latter is due to relatively small sensitivity of our simulations to moisture of extinction when $W_e \geq 0.6$.

The values of other parameters affect the results of our simulations markedly smaller than values of W_e. In particular, for all other governing parameters p, the range with a centre in $\mathcal{E}(p|D)$ and of width $4 \times \sigma(p|D)$ (for normal distributions, this corresponds to the 95 % confidence interval) is close to that for initial sampling range of this parameter (Table 1). The latter reflects a mutual redundancy between parameters. For instance, smaller k_{res} may be compensated by increased $m_{f,\,wood}$. Another example of this redundancy is compensation of smaller CO_2 emissions in the atmosphere (because of synergistic effect of k_{res} and $m_{f,\,wood}$) by enhanced carbon dioxide emissions from the peat fires.

We note, that the ensemble mean contribution of peat fires to the total CO_2 release in the atmosphere due to natural fires is small for all simulations reported in this paper.

BGD
11, 1443–1478, 2014

3.2 Present–day burnt area and CO_2 emissions

In our ensemble, the global present-day (1998–2011 AD) area burnt by natural fires is equal to $S_g = (2.1 \pm 0.4) \times 10^6\,km^2\,yr^{-1}$, and the respective CO_2 emissions are $E_g = 1.4 \pm 0.2\,PgC\,yr^{-1}$ (Table 2 and Fig. 2; here and below, the Bayesian ensemble mean and standard deviations are shown). The latter value agrees with the corresponding GFED–3.1 estimate $1.4 \pm 0.2\,PgC\,yr^{-1}$ (for the GFED data, we show interannual standard deviation). In different ensemble members, present-day S_g (E_g) changes from $0.8 \times 10^6\,km^2\,yr^{-1}$ to $5.8 \times 10^6\,km^2\,yr^{-1}$ (from $0.3\,PgC\,yr^{-1}$ to $3.3\,PgC\,yr^{-1}$). For ensemble members with $w_k \geq 1/K$ this range becomes markedly narrower: from $1.7 \times 10^6\,km^2\,yr^{-1}$ to $2.4 \times 10^6\,km^2\,yr^{-1}$ (from $1.2\,PgC\,yr^{-1}$ to $1.8\,PgC\,yr^{-1}$) (Figs. S7 and S8).

Present–day burnt area s per model grid cell ($4.5^\circ \times 6.0^\circ$ lat × lon) is typically between $5 \times 10^3\,km^2\,yr^{-1}$ and $10 \times 10^3\,km^2\,yr^{-1}$ (Fig. 3a). Regions with a substantial fire activity are simulated in most parts of Africa and South America, in the southern part of Asia, and in the boreal zone of Eastern Europe and Western Siberia. In these regions, there are hot spots with s which is up to $50 \times 10^3\,km^2\,yr^{-1}$. All regions with $s \geq 5 \times 10^3\,km^2\,yr^{-1}$ are characterised by a relatively narrow intra-ensemble uncertainty of present-day fire area, since here $\sigma(s|D)/\mathcal{E}(s|D) \leq 0.3$ (Fig. 3c).

Spatial distribution of carbon dioxide emissions due to natural fires per unit area of a grid cell, e, is a product of the burnt area, fuel stock, and its flammability. Maxima of these emissions are simulated in the tropics and subtropics, where both s and c_{fuel} are large. Here typically $e \geq 10\,gC\,m^{-2}\,yr^{-1}$ and they are frequently above $20\,gC\,m^{-2}\,yr^{-1}$ (Fig. 3b). However, despite the large burnt area in the Near East, emissions are relatively small here, attaining several $gC\,m^{-2}\,yr^{-1}$ because of the relatively small fuel stock in these regions. Sizeable emissions ($10\,gC\,m^{-2}\,yr^{-1} \leq e \leq 20\,gC\,m^{-2}\,yr^{-1}$) are simulated for boreal regions in northern Europe, West Siberia, north-eastern North America, and in Australia. In Europe, burnt area is small, but carbon dioxide emissions are noticeable. In most emissions–prone regions, $\sigma(e|D)/\mathcal{E}(e|D) \leq 0.3$ (Fig. 3d).

BGD
11, 1443–1478, 2014

Comparing to the GFED–3.1 data (Fig. 3d), the extent of regions serving as emission sources in the model is too large in the tropics and subtropics. In turn, tropical sources are underestimated, sometimes by a factor of five. In the middle latitudes, the model simulates most emission sources in the north-eastern part of Europe, while in the GFED data these emissions mostly come from the north-eastern part of Asia. This may be either a model bias or a reflection of the interannual variability in natural fire activity which our model is unable to reproduce. One reason for such a bias may be a neglect of fire suppression practice in our model. In particular, high population density and well developed infrastructure in Europe can efficiently suppress natural fires in this region (Kloster et al., 2010). An incorporation of dependence of ignition source on population density might be a route to improve our model. In turn, interannual variability of fire activity could result in emissions, which are larger than usual in eastern Asia in 1998–2011 relative to the previous years. We acknowledge that this point deserves future study.

Spatial distribution of the present-day burnt area and CO_2 emissions per grid cell in the tropics and subtropics changes little between different ensemble members with sufficiently large Bayesian weights (Figs. S7 and S8, left). We note, however, that there are ensemble members with a stronger emission source in the tropics (see the lowermost panels of these Figures as an example), while even in those members the tropical CO_2 source is still underestimated. Marked changes of the present-day s are found between such members in the boreal zone. For instance, clearly visible differences of this variable in boreal Eurasia are exhibited even for two ensemble members with the largest Bayesian weights: the ensemble member with $k = 4$ ($w_4 = 0.28$) and the member with $k = 15$ ($w_{15} = 0.32$). In particular, there are ensemble members with a weaker e in north-eastern Europe and stronger emissions in north-eastern Asia. The latter supports our notice that the discrepancy between the simulated and observed e is partly caused by interannual variability.

Averaged over the regions chosen by the GFED team (see Fig. S9 and http://globalfiredata.org/pics/Fig7_BasisregionsMap.jpg), the largest contribution to S_g is

BGD
11, 1443–1478, 2014

found for region MIDE (northern Africa and the Middle East; Table 2) with the next equally important contributions from region NHAF (the northern tropics of Africa; Fig. 4a) and from the combined region CEAS+EQAS+SEAS (which is the most part of Asia excluding boreal regions and the Middle east). The contribution of boreal regions (BOAS, which combines the Russian part of Asia and the northern part of European Russia, and BONA, which combines Canada and Alaska) to the present-day S_g is small. We note that the simulated present-day burnt area in the latter two regions ($(0.17 \pm 0.05) \times 10^6\,km^2\,yr^{-1}$ and $(0.07 \pm 0.02) \times 10^6\,km^2\,yr^{-1}$ correspondingly; Table 2) basically agrees with the numbers reported by (Conard et al., 2002) ($0.12 \times 10^6\,km^2\,yr^{-1}$ and $0.3 \times 10^6\,km^2\,yr^{-1}$ respectively). However, the correspondence between the GFED regions and the regions chosen by (Conard et al., 2002) is unclear. About one half of E_g comes from the regions SHSA (Africa southward from the equator), CEAS+EQAS+SEAS, and NHAF. Comparing with the GFED data, emissions from these regions are reproduced reasonably (see Fig. 4b) as an example. Another regions with an important contribution to E_g are TENA+CENA+NHSA (which combines the southern part of North America and the northern part of South America), MIDE, and SHAF (the southern tropics of Africa). However here the model strongly overestimates CO_2 emissions due to natural fires in the first two regions and strongly underestimates in the third one. For the boreal regions, BOAS and BONA, our model realistically simulates the present-day regionally–averaged annual CO_2 emissions (Table 2 and Fig. 4d and f). They also in a general agreement with the estimates by (Conard et al., 2002) (from $0.12\,PgC\,yr^{-1}$ to $0.19\,PgC\,yr^{-1}$ and from $0.03\,PgC\,yr^{-1}$ to $0.05\,PgC\,yr^{-1}$ respectively; the discrepancy for region BOAS may be caused by the above–mentioned imprecise correspondence of this region to the region chosen by (Conard et al., 2002)).

BGD
11, 1443–1478, 2014

3.3 Changes in the 21st century

In the end of the 21st century, the global burnt area increases to $(2.4 \pm 0.5) \times 10^6\,km^2\,yr^{-1}$ under scenario RCP 2.6, to $(2.7 \pm 0.5) \times 10^6\,km^2\,yr^{-1}$ under scenario RCP 4.5, to $(2.9 \pm 0.5) \times 10^6\,km^2\,yr^{-1}$ under scenario RCP 6.0, and to $(3.2 \pm 0.5) \times 10^6\,km^2\,yr^{-1}$ under scenario RCP 8.5 (Fig. 2a). These changes correspond to increases of the ensemble mean E_g relative to its value in 1998–2100 AD by 13 %, by 28 %, by 36 %, and by 51 % respectively. A proportional change is simulated for E_g which attains in year 2100 $1.6 \pm 0.3\,PgC\,yr^{-1}$ under scenario RCP 2.6, $1.9 \pm 0.3\,PgC\,yr^{-1}$ under scenario RCP 4.5, $2.0 \pm 0.3\,PgC\,yr^{-1}$ under scenario RCP 6.0, and $2.1 \pm 0.3\,PgC\,yr^{-1}$ under scenario RCP 8.5 (Fig. 2b). In relative units, the ensemble mean E_g is higher in 2100 AD with respect its value for years 1998–2011 by 14 % under scenario RCP 2.6, by 29 % under scenario RCP 4.5, by 37 % under scenario RCP 6.0, and by 42 % under scenario RCP 8.5.

For all scenarios, a general increase of the burnt area in the 21st century is caused by an increase of s on boreal regions of Eurasia and North America (Fig. 5, left panels). In particular, in the region BOAS, the ensemble mean burnt area is doubled during the 21st century under scenario RCP 2.6, tripled under scenario RCP 4.5, quadrupled under scenario RCP 6.0, and increased five–fold under scenario RCP 8.5 (Fig. 4b). A relative increase in the regions BOAS and EURO (the latter is the part of Europe excluding the former Soviet Union) is more modest. However, the year 2100 values of both S_{BOAS} and S_{EURO} are larger than the respective present-day values by more than one third under scenario RCP 2.6, and they are more than tripled under scenario RCP 8.5. In addition, under scenario RCP 8.5 there is a decrease of the burnt area in the northern tropics of Africa by about one third of its present-day value (Figs. 4a and 5e).

The most important contribution to the simulated increase of the burnt area in the boreal regions is given by an increase of the fire season length. The latter in our model depends on upper soil moisture content W (drier soil increases fire probability) and on fuel stock c_{fuel} (an increase of fuel stock makes easier to start the fire). In particular,

BGD
11, 1443–1478, 2014

in boreal North America, both soil drying and fuel stock increase in the 21st century simulated by the IAP RAS CM under all the RCP scenarios (Fig. 7a–d). In region BOAS, in contrast, soil as a whole becomes wetter during this century (while some grid cells with the decreasing W are visible in these regions in Fig. 7) and here increase of the burnt area is basically related to increase of c_{fuel}. The latter increase is responsible for the increase of S_{NHAF} as well. We note that the simulated increase of the fire season in boreal Eurasia length in the 21st century agrees with the results reported by Mokhov and Chernokulsky (2010) which were obtained by an application of fire danger index to the output of the regional climate model.

The direction of change of CO_2 emissions per unit area of a grid cell is rather similar to its burnt area counterpart (Fig. 6, left panels). In particular, the model simulates very pronounced enhancement of CO_2 emissions due to fires in boreal regions of Eurasia and North America. We note, however, that, in contrast to s, the region of the robust increase of e in the 21st century is simulated over the north-eastern part of Eurasia as well. This is caused by both the above–mentioned increase of the burnt area in these regions and by the respective increase of the carbon stock in living vegetation (the latter is reported by Mokhov and Eliseev, 2012) resulting in increased fuel stock. In addition, decrease of CO_2 emissions in the northern tropics of Africa in the 21st under scenario RCP 8.5 is less visible than its burnt area counterpart. This is a product of a diminished burnt area and an increased carbon stock in living vegetation.

Both the burnt area and release of the carbon dioxide in the atmosphere due to natural fires are quite robust within the studied ensemble. In particular, both Δs and Δe are similar between the ensemble members with sufficiently high Bayesian weights (Figs. S7 and S8, right panels).

3.4 Changes in the 22nd–23rd centuries

Under the mitigation scenario RCP 2.6, S_{g} and E_{g} start to decrease around year 2100, and reach in the late 23rd century $(2.3 \pm 0.5) \times 10^6\,\mathrm{km^2\,yr^{-1}}$ and $1.6 \pm 0.2\,\mathrm{PgC\,yr^{-1}}$ cor-

BGD
11, 1443–1478, 2014

respondingly (Fig. 2). Both values are decreased by about 5 % relative to their values in 2100 AD. Under other scenarios, both the burnt area and global CO_2 emissions form natural fires continue to increase. In our model, S_g achieves in year 2300 $(3.2 \pm 0.6) \times 10^6\,km^2\,yr^{-1}$ for scenario RCP 4.5, $(4.2 \pm 0.5) \times 10^6\,km^2\,yr^{-1}$ for scenario RCP 6.0, and $(5.9 \pm 0.5) \times 10^6\,km^2\,yr^{-1}$ for scenario RCP 8.5. This corresponds to the ensemble mean increase relative to the value in year 2100 by 15 % , 49 % and 83 %, respectively. In turn, E_g is increased by 9 % under scenario RCP 4.5, by 19 %, under scenario RCP 6.0, and by 31 % under scenario RCP 8.5. The simulated global CO_2 emissions from natural fires in the late 23rd century are $2.0 \pm 0.3\,PgC\,yr^{-1}$ for scenario RCP 4.5, $2.4 \pm 0.3\,PgC\,yr^{-1}$ for scenario RCP 6.0, and $2.7 \pm 0.3\,PgC\,yr^{-1}$ for scenario RCP 8.5.

In the 22nd–23rd centuries, the burnt area and carbon emissions due to natural fires increase further in boreal regions of Eurasia and North America for scenarios RCP 4.5, RCP 6.0, and RCP 8.5 (Figs. 5 and 6, right panels). This increase is more pronounced for scenarios with a higher anthropogenic carbon dioxide loading in the atmosphere. For the mitigation scenario RCP 2.6, however, in these regions the model simulates a slight decrease of the burnt area and respective carbon dioxide release in the atmosphere (Figs. 5b and 6b). The latter is reflected in the mentioned above small decrease of S_g and E_g under this scenario in this period. Under scenario RCP 8.5, a decrease of e is simulated in the subtropics of Eurasia. This increase is much less visible in change of s during these two centuries under the same scenario. As a result, this decrease of e is caused by a respective decrease of carbon stock in these regions.

In the vast region of boreal Eurasia, in the 22nd–23rd centiries our model simulates both soil drying and overall decrease of the vegetation carbon stock (Fig. 7e–h). As a result, during this period the burnt area in region BOAS increases due to climate changes, and the suppressed vegetation carbon stock counteracts this increase. The decreased vegetation carbon stock also leads to smaller relative increase of E_{BOAS} in comparison to that of S_{BOAS}. In region BONA, the changes of both these variables are not so pronounced as in Eurasia. This is the reason why relative increases of the burnt

BGD
11, 1443–1478, 2014

area and associated carbon dioxide emissions are smaller than their counterparts in region BOAS.

Similar to that obtained for the 21st century, our results are not very sensitive to specific details of the Bayesian weighting.

4 Conclusions

We performed simulations with the global climate model developed at the A. M. Obukhov Institute of Atmospheric Physics, Russian Academy of Sciences (IAP RAS CM). According to the CMIP5 experimental protocol, the model was forced by historical reconstruction of external forcings for 850–2005 AD and by the Representative Concentration Pathways (RCP) scenarios till year 2300. In contrast to other studies on a global-scale natural fire activity, our simulations were set up in an ensemble fashion. Different ensemble members were constructed by varying the governing parameters of the IAP RAS CM module to simulate natural fires. Further, these members are constrained by the GFED–3.1 observational data set and subjected to the Bayesian averaging. This approach allows to select only changes in fire characteristics which are robust within the constrained ensemble.

In our simulations, the present-day (1998–2011 AD) global area burnt due to natural fires is $(2.1 \pm 0.4) \times 10^6\,km^2\,yr^{-1}$ (the ensemble means and intra-ensemble standard deviations are presented), and the respective CO_2 emissions in the atmosphere are $(1.4 \pm 0.2)\,PgC\,yr^{-1}$. The latter value is in agreement with the corresponding observational estimates. Regionally, however, the model underestimates CO_2 emissions in the tropics; in the extra-tropics it underestimates these emissions in north-east Eurasia and overestimates them in Europe.

Our model simulates a drastic increase of the burnt area and the respective carbon dioxide emissions provided that anthropogenic forcing continues to grow in the next few centuries. In the 21st century, the ensemble mean global burnt area is increased by 13 % (28 %, 36 %, 51 %) under scenario RCP 2.6 (RCP 4.5, RCP 6.0, RCP 8.5). The

BGD
11, 1443–1478, 2014

corresponding global emissions increase is 14 % (29 %, 37 %, 42 %). In the 22nd–23rd centuries, under the mitigation scenario RCP 2.6, the ensemble mean global burnt area and respective CO_2 emissions slightly decrease, both by 5 % relative to their values in year 2100. They are continue to increase under other RCP scenarios. Under scenario RCP 8.5 (RCP 6.0, RCP 4.5), the ensemble mean burnt area in year 2300 is higher by 83 % (44 %, 15 %) than its value in year 2100, and the ensemble mean CO_2 emissions are correspondingly higher by 31 % (19 %, 9 %). All changes of natural fire characteristics in the 21st–23rd centuries are associated mostly with the corresponding changes in the boreal regions of Eurasia and North America. In particular, in boreal Eurasia and North America, an increase of both the ensemble mean burnt area and CO_2 emissions due to natural fires may be as large as several–fold. Under the RCP 8.5 scenario, an increase of the burnt area and CO_2 emissions in boreal regions during the 22nd–23rd centuries, however, is accompanied by the respective decrease in the tropics and subtropics.

Finally, we note that an enhancement of the carbon dioxide release in the atmosphere due to natural fires in the 21st–23rd centuries occurs under strong anthropogenic CO_2 emissions. For instance, an increase of E_g in the 21st century under the RCP 4.5 scenario by $0.2\,PgC\,yr^{-1}$ is just a 5 % of the fossil fuel+industrial carbon dioxide emissions which in this century rich $8\,PgC\,yr^{-1}$ under this scenario. Even smaller respective percentage is found for scenarios RCP 6.0 and RCP 8.5. As a result, an enhancement of e in the next several centuries unnder the RCP scenarios does not affect global characteristics of the carbon cycle. The latter may be used in the process of the development of international agreements similar to the Kyoto protocol.

Supplementary material related to this article is available online at http://www.biogeosciences-discuss.net/11/1443/2014/bgd-11-1443-2014-supplement.pdf.

BGD
11, 1443–1478, 2014

Acknowledgements. This work has been supported by the President of Russia grants 3894.2014.5 and 3895.2014.5, by the Russian Foundation for Basic Research, and by the Russian Academy of Sciences (programs of the Presidium RAS, programs by the Department of Earth Sciences RAS, and contract 74–OK/1–4).

References

Arora, V. and Boer, G.: Fire as an interactive component of dynamic vegetation models, J. Geophys. Res., 110, G02008, doi:10.1029/2005JG000042, 2005. 1445

Arzhanov, M., Eliseev, A., and Mokhov, I.: A global climate model based, Bayesian climate projection for northern extra–tropical land areas, Global Planet. Change, 86–87, 57–65, doi:10.1016/j.gloplacha.2012.02.001, 2012. 1453

Claussen, M., Mysak, L., Weaver, A., Crucifix, M., Fichefet, T., Loutre, M.-F., Weber, S., Alcamo, J., Alexeev, V., Berger, A., Calov, R., Ganopolski, A., Goosse, H., Lohmann, G., Lunkeit, F., Mokhov, I., Petoukhov, V., Stone, P., and Wang, Z.: Earth system models of intermediate complexity: closing the gap in the spectrum of climate system models, Clim. Dynam., 18, 579–586, doi:10.1007/s00382-001-0200-1, 2002. 1447

Conard, S., Sukhinin, A., Stocks, B., Cahoon, D., Davidenko, E., and Ivanova, G.: Determistic effects of area burned and fire severity on carbon cycling and emissions in Siberia, Climatic Change, 55, 197–211, doi:10.1023/A:1020207710195, 2002. 1454, 1458

de Groot, W. J. and Field, R., Brady, M., Roswintiarti, O., and Mohamad, M.: Development of the Indonesian and Malaysian fire danger rating systems, Mitig. Adapt. Strat. Glob. Change, 12, 165–180, doi:10.1007/s11027-006-9043-8, 2007. 1445

Dowdy, A., Mills, G., Finkele, K., and de Groot, W.: Index sensitivity analysis applied to the Canadian Forest Fire Weather Index and the McArthur Forest Fire Danger Index, Meteorol. Appl., 17, 298–312, doi:10.1002/met.170, 2010. 1445

Eby, M., Weaver, A. J., Alexander, K., Zickfeld, K., Abe-Ouchi, A., Cimatoribus, A. A., Crespin, E., Drijfhout, S. S., Edwards, N. R., Eliseev, A. V., Feulner, G., Fichefet, T., Forest, C. E., Goosse, H., Holden, P. B., Joos, F., Kawamiya, M., Kicklighter, D., Kienert, H., Matsumoto, K., Mokhov, I. I., Monier, E., Olsen, S. M., Pedersen, J. O. P., Perrette, M., Philippon-Berthier, G., Ridgwell, A., Schlosser, A., Schneider von Deimling, T., Shaffer, G., Smith, R. S., Spahni, R., Sokolov, A. P., Steinacher, M., Tachiiri, K., Tokos, K., Yoshimori, M., Zeng, N.,

BGD
11, 1443–1478, 2014

and Zhao, F.: Historical and idealized climate model experiments: an intercomparison of Earth system models of intermediate complexity, Clim. Past, 9, 1111–1140, doi:10.5194/cp-9-1111-2013, 2013. 1447
Eliseev, A.: Estimation of the uncertainty of future changes in atmospheric carbon dioxide concentration and its radiative forcing, Izvestiya, Atmos. Ocean. Phys., 44, 279–287, doi:10.1134/S0001433808030031, 2008. 1453
Eliseev, A.: Estimation of changes in characteristics of the climate and carbon cycle in the 21st century accounting for the uncertainty of terrestrial biota parameter values, Izvestiya, Atmos. Ocean. Phys., 47, 131–153, doi:10.1134/S0001433811020046, 2011. 1453
Eliseev, A.: Climate change mitigation via sulfate injection to the stratosphere: impact on the global carbon cycle and terrestrial biosphere, Atmos. Ocean. Opt., 25, 405–413, doi:10.1134/S1024856012060024, 2012. 1447
Eliseev, A. and Mokhov, I.: Uncertainty of climate response to natural and anthropogenic forcings due to different land use scenarios, Adv. Atmos. Sci., 28, 1215–1232, doi:10.1007/s00376-010-0054-8, 2011. 1447
Eliseev, A. and Sergeev, D.: Impact of subgrid–scale heterogeneity of vegetation on the results of simulation of carbon cycle characteristics, Izvestiya, Atmos. Ocean Phys., 50, in press, 2014. 1447, 1448
Eliseev, A. V., Coumou, D., Chernokulsky, A. V., Petoukhov, V., and Petri, S.: Scheme for calculation of multi-layer cloudiness and precipitation for climate models of intermediate complexity, Geosci. Model Dev., 6, 1745–1765, doi:10.5194/gmd-6-1745-2013, 2013. 1455
Greene, A., Goddard, L., and Lall, U.: Probabilistic multimodel regional temperature change projections, J. Climate, 19, 4326–4343, doi:10.1175/JCLI3864.1, 2006. 1453
Hoeting, J., Madigan, D., Raftery, A., and Volinsky, C.: Bayesian model averaging: a tutorial, Stat. Sci., 14, 382–401, 1999. 1450, 1453
Houghton, R. A., House, J. I., Pongratz, J., van der Werf, G. R., DeFries, R. S., Hansen, M. C., Le Quéré, C., and Ramankutty, N.: Carbon emissions from land use and land-cover change, Biogeosciences, 9, 5125–5142, doi:10.5194/bg-9-5125-2012, 2012. 1454
Kass, R. and Raftery, A.: Bayes factors, J. Am. Stat. Assoc., 90, 773–795, 1995. 1450, 1453
Kattsov, V., Walsh, J., Chapman, W., Govorkova, V., Pavlova, T., and Zhang, X.: Simulation and projection of Arctic freshwater budget components by the IPCC AR4 global climate models, J. Hydrometeorol., 8, 571–589, doi:10.1175/JHM575.1, 2007. 1453

BGD
11, 1443–1478, 2014

Khon, V., Mokhov, I., Latif, M., Semenov, V., and Park, W.: Perspectives of Northern Sea Route and Northwest Passage in the twenty–first century, Climatic Change, 100, 757–768, doi:10.1007/s10584-009-9683-2, 2010. 1453

Kloster, S., Mahowald, N. M., Randerson, J. T., Thornton, P. E., Hoffman, F. M., Levis, S., Lawrence, P. J., Feddema, J. J., Oleson, K. W., and Lawrence, D. M.: Fire dynamics during the 20th century simulated by the Community Land Model, Biogeosciences, 7, 1877–1902, doi:10.5194/bg-7-1877-2010, 2010. 1445, 1457

Kloster, S., Mahowald, N. M., Randerson, J. T., and Lawrence, P. J.: The impacts of climate, land use, and demography on fires during the 21st century simulated by CLM-CN, Biogeosciences, 9, 509–525, doi:10.5194/bg-9-509-2012, 2012. 1445

Leroy, S.: Detecting climate signals: some Bayesian aspects, J. Climate, 11, 640–651, 1998. 1450, 1453

Li, F., Zeng, X. D., and Levis, S.: A process-based fire parameterization of intermediate complexity in a Dynamic Global Vegetation Model, Biogeosciences, 9, 2761–2780, doi:10.5194/bg-9-2761-2012, 2012. 1445

McKay, M., Beckman, R., and Conover, W.: A comparison of three methods for selecting values of input variables in the analysis of output from a computer code, Technometrics, 21, 239–245, 1979. 1450

Mokhov, I. and Chernokulsky, A.: Regional model assessments of forest fire risks in the asian part of Russia under climate change, Geogr. Nat. Resour., 31, 165–169, doi:10.1016/j.gnr.2010.06.012, 2010. 1446, 1460

Mokhov, I. and Eliseev, A.: Modeling of global climate variations in the 20th–23rd centuries with new RCP scenarios of anthropogenic forcing, Dokl. Earth Sci., 443, 532–536, doi:10.1134/S1028334X12040228, 2012. 1447, 1460

Mokhov, I., Demchenko, P., Eliseev, A., Khon, V., and Khvorostyanov, D.: Estimation of global and regional climate changes during the 19th–21st centuries on the basis of the IAP RAS model with consideration for anthropogenic forcing, Izvestiya, Atmos. Ocean. Phys., 38, 555–568, 2002. 1447

Mokhov, I., Eliseev, A., Demchenko, P., Khon, V., Akperov, M., Arzhanov, M., Karpenko, A., Tikhonov, V., Chernokulsky, A., and Sigaeva, E.: Climate changes and their assessment based on the IAP RAS global model simulations, Dokl. Earth Sci., 402, 591–595, 2005. 1447

BGD
11, 1443–1478, 2014

Mokhov, I., Chernokulsky, A., and Shkolnik, I.: Regional model assessments of fire risks under global climate changes, Dokl. Earth Sci., 411, 1485–1488, doi:10.1134/S1028334X06090340, 2006. 1445

Moss, R., Edmonds, J., Hibbard, K., Manning, M., Rose, S., van Vuuren, D., Carter, T., Emori, S., Kainuma, M., Kram, T., Meehl, G., Mitchell, J., Nakicenovic, N., Riahi, K., Smith, S., Stouffer, R., Thomson, A., Weyant, J., and Wilbanks, T.: The next generation of scenarios for climate change research and assessment, Nature, 463, 747–756, doi:10.1038/nature08823, 2010. 1449

Nesterov, V.: Flammability of Forest and Approaches for its Estimation, Gidrometeoizdat, Leningrad, 1949 (in Russian). 1446

Noble, I., Gill, A., and Bary, G.: McArthur's fire–danger meters expressed as equations, Aust. J. Ecol., 5, 201–203, doi:10.1111/j.1442-9993.1980.tb01243.x, 1980. 1446

Pechony, O. and Shindell, D.: Fire parameterization on a global scale, J. Geophys. Res., 114, D16115, doi:10.1029/2009JD011927, 2009. 1445

Petoukhov, V., Mokhov, I., Eliseev, A., and Semenov, V.: The IAP RAS Global Climate Model, Dialogue–MSU, Moscow, 1998. 1447

Petoukhov, V., Claussen, M., Berger, A., Crucifix, M., Eby, M., Eliseev, A., Fichefet, T., Ganopolski, A., Goosse, H., Kamenkovich, I., Mokhov, I., Montoya, M., Mysak, L., Sokolov, A., Stone, P., Wang, Z., and Weaver, A.: EMIC intercomparison project (EMIP–CO2): comparative analysis of EMIC simulations of current climate and equilibrium and transient reponses to atmospheric CO_2 doubling, Clim. Dynam., 25, 363–385, doi:10.1007/s00382-005-0042-3, 2005. 1447

Sitch, S., Smith, B., Prentice, I., Arneth, A., Bondeau, A., Cramer, W., Kaplan, J., Levis, S., Lucht, W., Sykes, M., Thonicke, K., and Venevsky, S.: Evaluation of ecosystem dynamics, plant geography and terrestrial carbon cycling in the LPJ dynamic global vegetation model, Glob. Change Biol., 9, 161–185, doi:10.1046/j.1365-2486.2003.00569.x, 2003. 1445

Stein, M.: Large sample properties of simulations using latin hypercube sampling, Technometrics, 29, 141–150, doi:10.2307/1269769, 1987. 1450

Taylor, K.: Summarizing multiple aspects of model performance in a single diagram, J. Geophys. Res., 106, 7183–7192, doi:10.1029/2000JD900719, 2001. 1452

Taylor, K., Stouffer, R., and Meehl, G.: An overview of CMIP5 and the experiment design, B. Am. Meteorol. Soc., 93, 485–498, doi:10.1175/BAMS-D-11-00094.1, 2012. 1446, 1449

BGD
11, 1443–1478, 2014

Thonicke, K., Venevsky, S., Sitch, S., and Cramer, W.: The role of fire disturbance for global vegetation dynamics: coupling fire into a Dynamic Global Vegetaion Model, Glob. Ecol. Biogeogr., 10, 661–677, 2001. 1445, 1448

Thonicke, K., Spessa, A., Prentice, I. C., Harrison, S. P., Dong, L., and Carmona-Moreno, C.: The influence of vegetation, fire spread and fire behaviour on biomass burning and trace gas emissions: results from a process-based model, Biogeosciences, 7, 1991–2011, doi:10.5194/bg-7-1991-2010, 2010. 1445

van der Werf, G. R., Randerson, J. T., Giglio, L., Collatz, G. J., Mu, M., Kasibhatla, P. S., Morton, D. C., DeFries, R. S., Jin, Y., and van Leeuwen, T. T.: Global fire emissions and the contribution of deforestation, savanna, forest, agricultural, and peat fires (1997–2009), Atmos. Chem. Phys., 10, 11707–11735, doi:10.5194/acp-10-11707-2010, 2010. 1452

Van Wagner, C.: Development and Structure of the Canadian Forest Fire Weather Index System, Tech. Rep. 35, Canadian Forestry Service, Ottawa, 1987. 1446

Zickfeld, K., Eby, M., Weaver, A., Alexander, K., Crespin, E., Edwards, N., Eliseev, A., Feulner, G., Fichefet, T., Forest, C., Friedlingstein, P., Goosse, H., Holden, P., Joos, F., Kawamiya, M., Kicklighter, D., Kienert, H., Matsumoto, K., Mokhov, I., Monier, E., Olsen, S., Pedersen, J., Perrette, M., Philippon-Berthier, G., Ridgwell, A., Schlosser, A., Schneider von Deimling, T., Shaffer, G., Sokolov, A., Spahni, R., Steinacher, M., Tachiiri, K., Tokos, K., Yoshimori, M., Zeng, N., and Zhao, F.: Long–term climate change commitment and reversibility: an EMIC intercomparison, J. Climate, 26, 5782–5809, doi:10.1175/JCLI-D-12-00584.1, 2013. 1447

BGD
11, 1443–1478, 2014

Table 1. Standard values, sampling ranges, and posterior distributions of variables varied within the ensemble constructed in this paper. In the first column, "ND" stands for "non–dimensional". The plant functional types (PFTs) are: TT – tropical trees, EDT – extra–tropical deciduous trees, ENT – extra–tropical evergreen (needle–leaf) trees, GRA – grasses, SHR – shrubs, WTL – bogs/mires/fens, CRO – crops. Long dashes in the last two columns indicate that respective parameter is not sampled for a given PFT.

variable	PFTs	standard value	sampling range	posterior distribution
$c_{\mathrm{fuel},0}$, $\mathrm{kgC\,m^{-2}}$	all	0.2	0.1–0.3	0.21 ± 0.07
W_{e}, ND	all	0.7	0.4–0.8	0.56 ± 0.03
$m_{\mathrm{f,\,wood}}$, ND	all	0.2	0.15–0.50	0.36 ± 0.10
k_{res}, ND	TT, EDT	0.5	0.25–0.75	0.51 ± 0.10
	ENT, SHR, WTL	0.12	0.1–0.2	0.15 ± 0.04
	CRO	0.1	0–0.2	0.12 ± 0.05
	GRA	1	–	–
$\alpha_{\mathrm{f,\,s}}$, ND	WTL	2	0–4	2.1 ± 0.8
	all other	0	–	–

BGD
11, 1443–1478, 2014

Table 2. Characteristics of natural fires in the simulations with the IAP RAS CM. For each variable, the burnt area S and CO_2 emissions in the atmosphere E, the Bayesian ensemble mean and standard deviation are shown. The values for S are in $10^6\,km^2\,yr^{-1}$, and for E they are in $PgC\,yr^{-1}$. The regions correspond to classification used by the GFED team as shown in Fig. S9. For years 1998–2011, GFED–3.1 estimates (mean and interannual standard deviations) are shown in brackets.

var	1998–2011	2090–2100			
		RCP 2.6	RCP 4.5	RCP 6.0	RCP 8.5
		global			
S	2.1 ± 0.4	2.4 ± 0.5	2.7 ± 0.5	2.9 ± 0.5	3.2 ± 0.5
E	1.4 ± 0.2 (1.4 ± 0.2)	1.6 ± 0.3	1.9 ± 0.3	2.0 ± 0.3	2.1 ± 0.3
		BOAS			
S	0.17 ± 0.05	0.35 ± 0.08	0.55 ± 0.07	0.66 ± 0.09	1.00 ± 0.07
E	0.07 ± 0.02 (0.11 ± 0.09)	0.14 ± 0.03	0.22 ± 0.04	0.28 ± 0.06	0.39 ± 0.07
		CEAS+SEAS+EQAS			
S	0.35 ± 0.06	0.38 ± 0.07	0.39 ± 0.08	0.39 ± 0.08	0.40 ± 0.08
E	0.25 ± 0.04 (0.10 ± 0.05)	0.28 ± 0.05	0.29 ± 0.05	0.30 ± 0.05	0.31 ± 0.05
		AUST			
S	0.17 ± 0.03	0.17 ± 0.03	0.17 ± 0.03	0.17 ± 0.03	0.16 ± 0.03
E	0.08 ± 0.01 (0.12 ± 0.04)	0.08 ± 0.01	0.08 ± 0.01	0.08 ± 0.01	0.08 ± 0.01
		BONA			
S	0.07 ± 0.02	0.11 ± 0.03	0.13 ± 0.03	0.18 ± 0.03	0.21 ± 0.05
E	0.05 ± 0.01 (0.05 ± 0.03)	0.08 ± 0.02	0.11 ± 0.02	0.12 ± 0.02	0.14 ± 0.03
		TENA+CENA+NHSA			
S	0.20 ± 0.05	0.21 ± 0.05	0.21 ± 0.05	0.21 ± 0.05	0.21 ± 0.05
E	0.18 ± 0.06 (0.03 ± 0.02)	0.20 ± 0.06	0.21 ± 0.07	0.22 ± 0.07	0.22 ± 0.07
		SHSA			
S	0.24 ± 0.04	0.24 ± 0.04	0.24 ± 0.04	0.24 ± 0.04	0.24 ± 0.04
E	0.26 ± 0.04 (0.12 ± 0.06)	0.28 ± 0.05	0.29 ± 0.05	0.30 ± 0.05	0.30 ± 0.05
		EURO			
S	0.04 ± 0.01	0.05 ± 0.01	0.07 ± 0.01	0.09 ± 0.02	0.11 ± 0.02
E	0.02 ± 0.01 (0.01 ± 0.01)	0.04 ± 0.01	0.05 ± 0.01	0.05 ± 0.01	0.06 ± 0.01

BGD
11, 1443–1478, 2014

Table 2. Continued.

var	1998–2011	2090–2100			
		RCP 2.6	RCP 4.5	RCP 6.0	RCP 8.5
		MIDE			
S	0.44 ± 0.12	0.46 ± 0.14	0.51 ± 0.15	0.51 ± 0.13	0.48 ± 0.14
E	0.14 ± 0.02 (0.001 ± 0.001)	0.15 ± 0.02	0.17 ± 0.02	0.17 ± 0.03	0.16 ± 0.03
		NHAF			
S	0.32 ± 0.05	0.31 ± 0.05	0.32 ± 0.05	0.34 ± 0.06	0.28 ± 0.05
E	0.23 ± 0.03 (0.38 ± 0.06)	0.24 ± 0.03	0.26 ± 0.03	0.29 ± 0.04	0.22 ± 0.03
		SHAF			
S	0.14 ± 0.03	0.14 ± 0.03	0.14 ± 0.03	0.14 ± 0.03	0.14 ± 0.03
E	0.15 ± 0.03 (0.49 ± 0.04)	0.16 ± 0.03	0.17 ± 0.04	0.17 ± 0.04	0.17 ± 0.04

BGD
11, 1443–1478, 2014

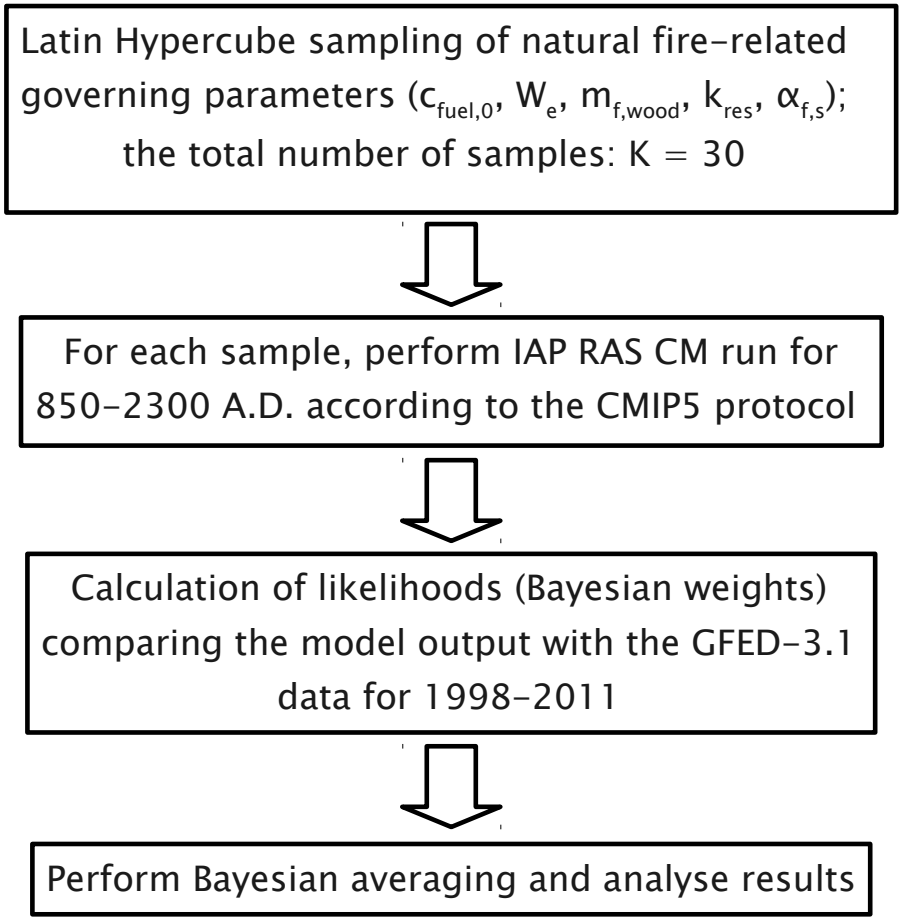

Fig. 1. The general flow chart.

BGD
11, 1443–1478, 2014

a)

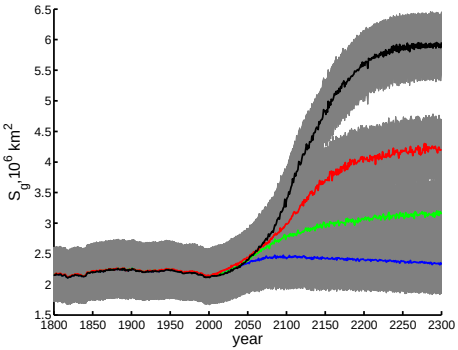

b)

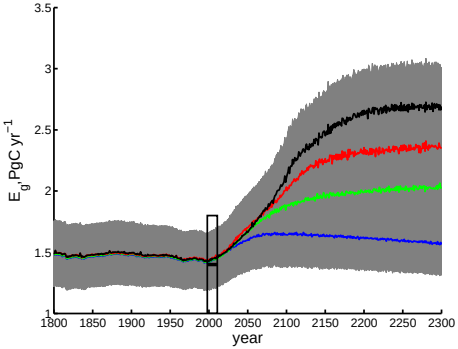

Fig. 2. Ensemble mean global natural fires burnt area **(a)** and respective CO_2 emissions to the atmosphere **(b)** in the simulations RCP 2.6, RCP 4.5, RCP 6.0, and RCP 8.5 (blue, green red, and black curves correspondingly) together with intra-ensemble standard deviations (gray shading). The rectangle in **(b)** represents the GFED–3.1 observations (mean and interannual standard deviation).

BGD
11, 1443–1478, 2014

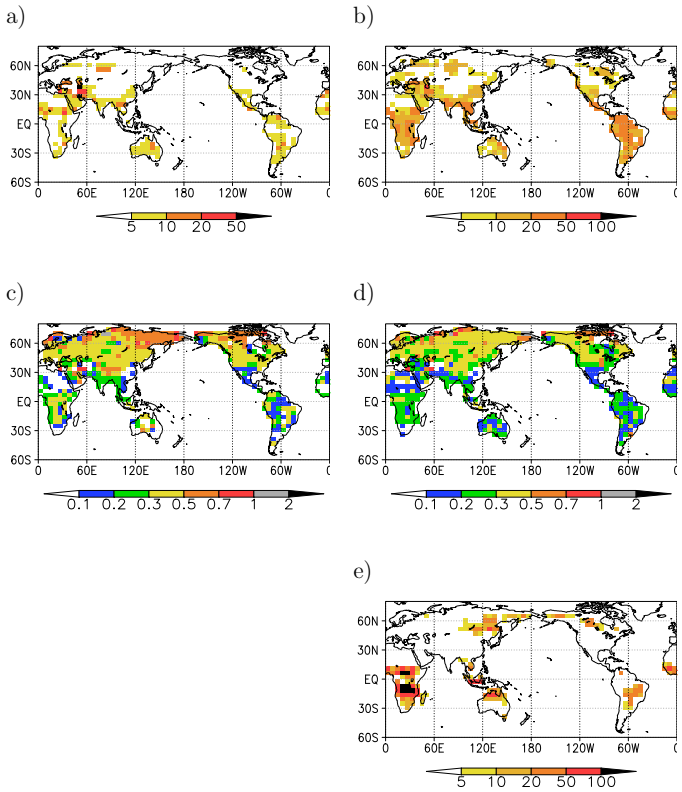

Fig. 3. Area annually burnt by natural fires (**a** and **c**), and corresponding CO_2 emissions in the atmosphere (**b** and **d**) simulated by the IAP RAS CM for years 1998–2011. Shown are the Bayesian ensemble means (burnt area: $10^3\,km^2\,yr^{-1}$ per grid cell **(a)** and emissions in $gC\,m^{-2}\,yr^{-1}$) **(b)** and the ratios of the Bayesian standard deviations to the Bayesian ensemble means **(c)** and **(d)**. In addition, GFED–3.1 observation for CO_2 emissions due to natural fires are shown in **(e)**.

BGD
11, 1443–1478, 2014

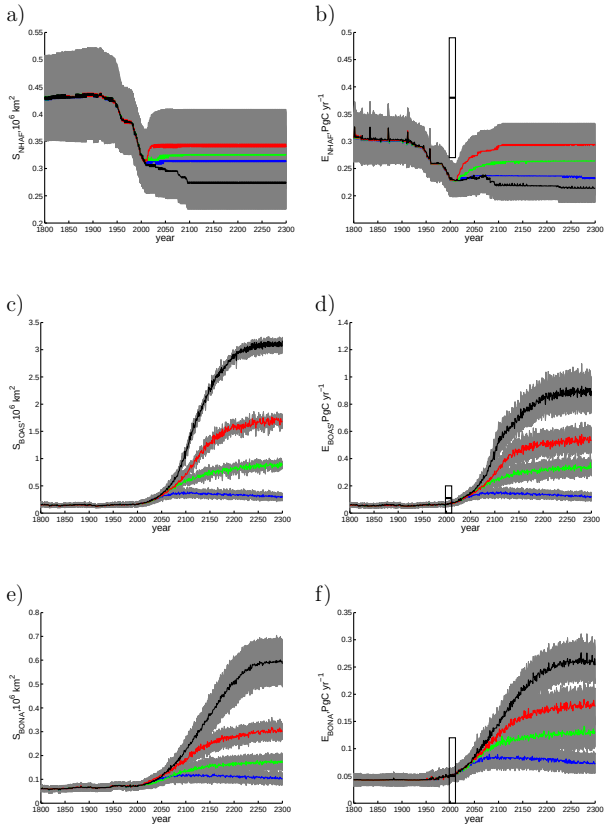

Fig. 4. Similar to Fig. 2, but for the burnt area (**a**, **c**, and **e**) and respective CO_2 emissions (**b**, **d**, and **f**) summed over the GFED regions NHAF (**a** and **b**), BOAS (**c** and **d**), and BONA (**e** and **f**). GFED regions are shown in Fig. S9.

BGD
11, 1443–1478, 2014

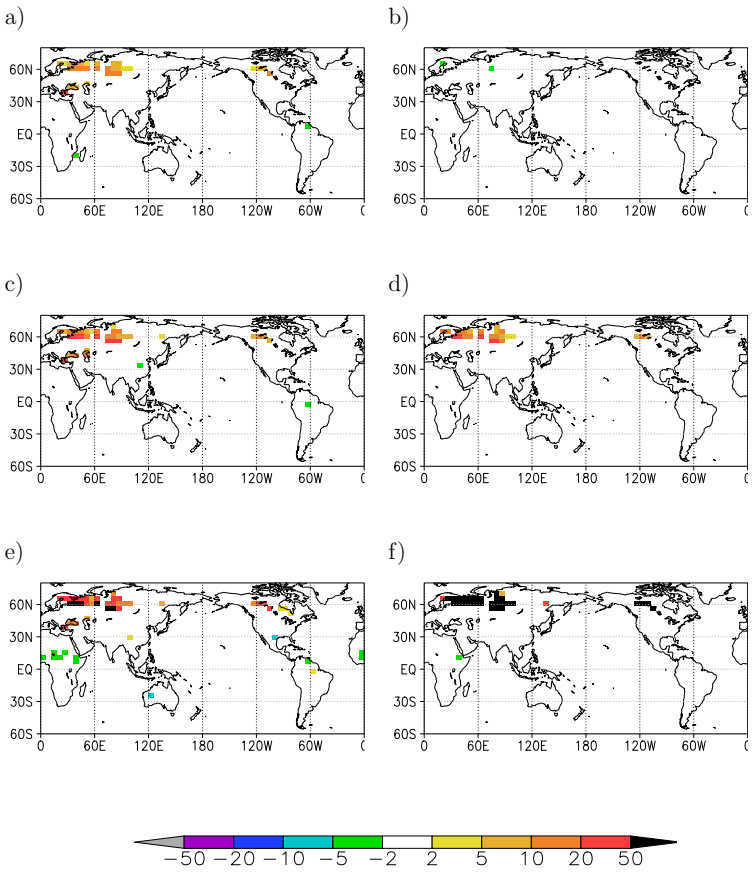

Fig. 5. Change of the area annually burnt by natural fires (10^3 km^2 yr^{-1} per grid cell) from 1998–2011 AD to 2090–2100 AD (**a**, **c**, and **e**) and from 2090–2100 AD to 2290–2300 AD (**b**, **d**, and **f**) in simulations RCP 2.6 (**a** and **b**), RCP 4.5 (**c** and **d**), and RCP 8.5 (**e** and **f**).

BGD
11, 1443–1478, 2014

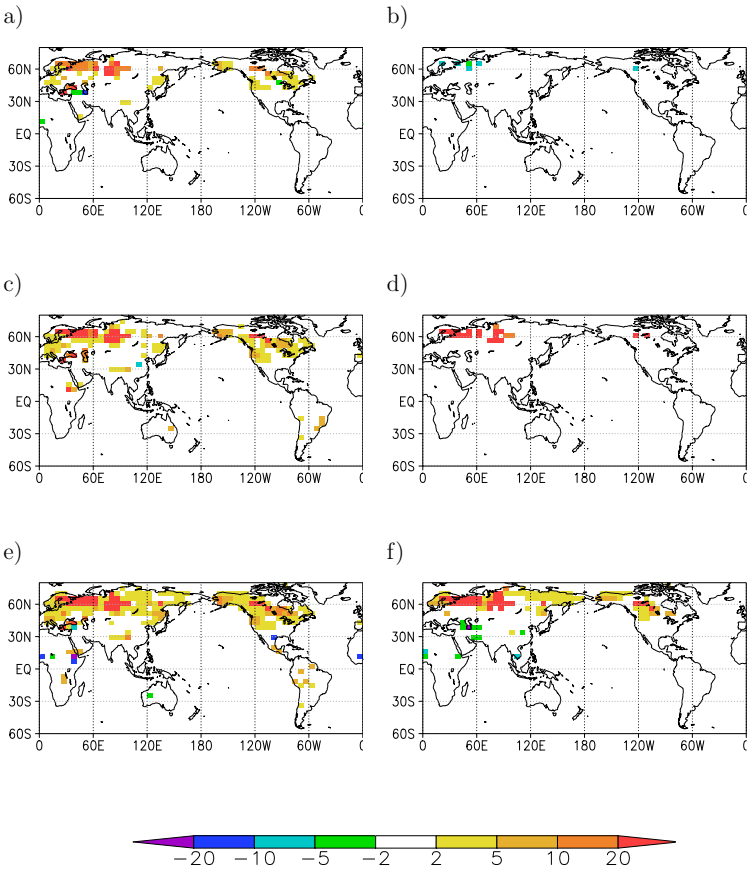

Fig. 6. Similar to Fig. 5, but for the corresponding CO_2 emissions in the atmosphere ($gC\,m^{-2}\,yr^{-1}$).

BGD
11, 1443–1478, 2014

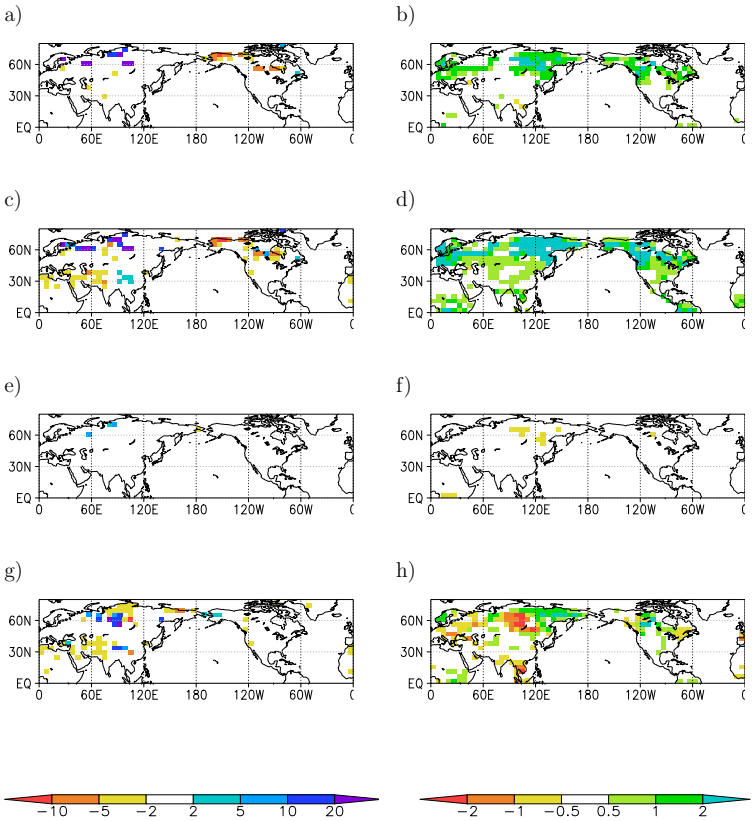

Fig. 7. Change of the moisture content of the upper 5 cm of soil (in cm(water) m(soil)$^{-1}$; **a**, **c**, **e**, and **g**) and of the vegetation carbon stock (kgC m^{-2} **b**, **d**, **f**, and **h**) from 1998–2011 to 2091–2100 (**a–d**) and from 2091–2100 to 2291–2300 (**e–h**) for scenarios RCP 2.6 (**a**, **b**, **e**, and **f**) and RCP 8.5 (**c**, **d**, **g**, and **h**).

BGD
11, 1443–1478, 2014